




# Nanoporous SiO<sub>2</sub> based on annealed artificial opals as a favorable material platform of terahertz optics

V. E. ULITKO,<sup>1,6</sup> A. K. ZOTOV,<sup>1</sup> A. A. GAVDUSH,<sup>2</sup> G. M. KATYBA,<sup>1,2</sup> G. A. KOMANDIN,<sup>2</sup>  I. E. SPEKTOR,<sup>2</sup> I. M. SHMYTKO,<sup>1</sup> G. A. EMELCHENKO,<sup>1</sup> I. N. DOLGANOVA,<sup>1,3</sup>  M. SKOROBOGATIY,<sup>4,7</sup> V. N. KURLOV,<sup>1,3,8</sup> V. M. MASALOV,<sup>1</sup> AND K. I. ZAYTSEV<sup>2,3,5,9</sup> 

<sup>1</sup>*Institute of Solid State Physics of the Russian Academy of Sciences, Academica Osipyana str. 2, Chernogolovka 142432, Russia*

<sup>2</sup>*Prokhorov General Physics Institute of the Russian Academy of Sciences, Vavilova str. 38, Moscow 119991, Russia*

<sup>3</sup>*Institute for Regenerative Medicine, Sechenov First Moscow State Medical University (Sechenov University), Bolshaya Pirogovskaya str. 19/1, Moscow 119146, Russia*

<sup>4</sup>*Department of Engineering Physics, Polytechnique Montreal, 2500 Chemin de Polytechnique, Montréal, QC H3T 1J4, Canada*

<sup>5</sup>*Bauman Moscow State Technical University, 2nd Baumanskaya str., Moscow 105005, Russia*

<sup>6</sup>*ulitko.vl@gmail.com*

<sup>7</sup>*maksim.skorobogatiy@polymtl.ca*

<sup>8</sup>*kurlov@issp.ac.ru*

<sup>9</sup>*kirzay@gmail.com*

**Abstract:** In this paper, artificial opals, made of 300-nm-diameter nanoporous SiO<sub>2</sub> globules by sedimentation of a colloidal suspension and annealing at different temperatures in the range of 200–1500 °C, are studied as a promising material platform for terahertz (THz) optics. Our findings reveal that THz optical properties of such materials can be predictably varied in a wide range by annealing, while being a deterministic function of the material porosity. Thus, when increasing annealing temperature, the resultant material refractive index increases from 1.65 to 1.95 at 1.0 THz, while the material absorption coefficient (by field) reduces from 10 to 1 cm<sup>-1</sup>. The Bruggeman effective medium theory was then successfully applied to model optical properties of the nanoporous SiO<sub>2</sub> at THz frequencies as a function of the material porosity and the annealing temperature. Finally, bulk nanoporous SiO<sub>2</sub> were shaped using conventional grinding techniques into plates and cylindrical lenses to demonstrate robustness of the novel THz optical materials. A wide range of the nanoporous SiO<sub>2</sub> refractive indices, their low-to-moderate THz-wave absorption, as well as their mechanical robustness make such materials a promising platform for THz optics.

© 2020 Optical Society of America under the terms of the [OSA Open Access Publishing Agreement](#)

## 1. Introduction

Over the past few decades, THz spectroscopy and imaging [1] attracted considerable attention, as a promising tools for solving numerous demanding problems in astrophysics and astrochemistry [2,3], condensed matter physics [4,5], biology and medicine [6,7], security task [8], materials science and non-destructive testing [9], quality control in chemical and pharmaceutical industries [10], and food science [11]. Despite such a progress, THz science remains quite a novel branch of applied physics that can still profit from a variety of advanced opto-electronic components, optical systems, and materials [12–16]. This need pushes further development of the novel effective THz optical materials and related fabrication technologies [17,18].

Currently, only a limited number of polymer and crystalline materials exist that are suitable for application in the THz range. Such materials are typically chosen for their small-to-moderate group velocity dispersion and low electromagnetic-wave absorption [19–21]. Among the common THz polymers [20], High/Low-Density PolyEthylene (HDPE/LDPE), PolyTetraFluoroEthylene (PTFE/Teflon), PolyMethylPentene (PMP/TPX), Biaxially-Oriented PolyEthylene Terephthalate (BoPET/Mylar), and Cyclo Olefin Polymer (COP/Zeonor) should be mentioned. Most polymer materials allow fabrication of THz optical components via mechanical processing, while some of them can be processed by drawing, compression molding, or even 3D printing in order to form complex-shaped optical elements [22–31]. Among the THz crystalline materials [19], we should mention High-Resistivity Float-Zone silicon (HRFZ-Si), crystalline quartz, sapphire ( $\alpha$ -Al<sub>2</sub>O<sub>3</sub>), and diamond grown using Chemical Vapor Deposition (CVD) method. These crystals are quite hard in synthesis and mechanically process due to high hardness and (in some cases) anisotropy of their physical properties, thus, increasing cost and limiting their reliability. This difficulty can be partially mitigated for sapphire using the Edge-defined Film-fed Growth (EFG) technique [32–34], which yields fabrication of sapphire crystals with a complex predetermined cross-section geometry and high volumetric and surface quality directly from the Al<sub>2</sub>O<sub>3</sub>-melt [35]. This technique was applied to fabrication of the hollow-core THz waveguides [36], flexible step-index THz optical fibers and fiber bundles [37,38]. Nevertheless, such a crystal growth technique seems to be sub-optimal for the fabrication of bulk THz optical components.

One promising way to overcome the lack of THz optical materials is using artificial or natural composites, the optical response of which can be tuned by modifying their chemical composition, phase state, or structural properties. In Ref. [39–43], composites made of natural stones, mixtures of polymer and crystalline powders, and wood-plastic structures were applied as materials with a wide adjustability of THz optical properties. Nevertheless, their fabrication remains a daunting, time-consuming, and expensive task, while their residual micro-scale structural inhomogeneities might lead to additional losses and scattering of the THz-beam power. In Refs. [26,30], spatially variable sub-wavelength porosity and additive manufacturing were exploited to design THz optical components such as lenses and phase plates. This approach can yield a wide variety of advanced THz optical elements, but requires high-resolution 3D printers and generally lacks low loss materials compatible with additive manufacturing, in order to suppress THz-wave scattering and absorption losses. In Ref. [44–46], effective THz optical properties of porous silk foams, silica aerogels, and SiO<sub>2</sub> glass were studied. Such materials are potentially suitable for THz optics, however, they remain sub-optimal for many applications due to either a very low refractive index or a high THz-wave absorption. In Refs. [47–49], a wire medium, i.e. an array of metal wires, suspended in a free space or embedded into a dielectric material, was considered, with a strong potential for the near-field imaging. Despite the advanced spatial resolution, a wire medium possesses a limited practical reliability due to significant THz-wave losses and inter-wire cross talk. Finally, in Refs. [50,51], laser direct-written all-carbon THz optical materials and related fabrication technology were introduced. Such materials hold strong potential for THz optics, however yield only planar optical elements. Thus, while many novel techniques were developed for the fabrication of bulk THz optical components, they are still somewhat exotic, each one of them occupying a respective application niche.

In this work, a novel robust material platform for THz optics that is compatible with most mechanical processing techniques is considered – namely, artificial opals [52–54]. These are based on 300-nm-diameter nanoporous SiO<sub>2</sub> globules and are fabricated by sedimentation of a colloidal suspension, followed by annealing at the temperatures of 200–1500 °C. Experimental studies of such materials, using THz pulsed spectroscopy, revealed strong dependence of their porosity and related effective THz optical properties on the annealing conditions. Particularly, porous material's refractive indices and absorption coefficients (by field) at 1.0 THz change from 1.65 to 1.95 and from 10 to 1 cm<sup>-1</sup>, respectively, depending on the annealing temperatures.

Observed values of the complex refractive index can be described as a function of the material porosity and the annealing temperature using the Bruggeman effective medium model. The developed material platform is mechanically robust and allows fabrication of the bulk optical elements using conventional mechanical processing. The ability to design the optical properties of nanoporous SiO<sub>2</sub>, together with its mechanical robustness make such materials attractive for THz optics.

## 2. Nanoporous SiO<sub>2</sub> based on annealed opals

Bulk opal samples were made using monodispersed spherical nanoporous SiO<sub>2</sub> particles with the diameter of 300 nm. They feature the Face Centered Cubic (FCC) lattice, the schematic and the Scanning Electron Microscopy (SEM) images of which are shown in Fig. 1. The latter were obtained with Zeiss Supra 50 VP SEM system.

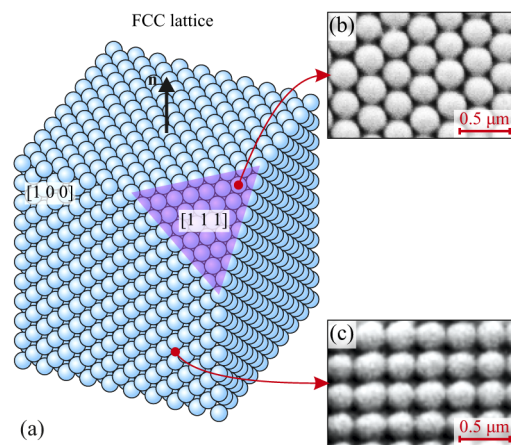


**Fig. 1.** The opal crystal formed by the nanoporous SiO<sub>2</sub> globules. (a) Schematic of the opal crystal featuring the FCC lattice. (b),(c) SEM images of the opal crystallographic planes [100] and [111].

For the synthesis of SiO<sub>2</sub> nanoparticles, TetraEthOxySilane (TEOS, 98%) preliminary purified by rectification, CycloHexane (CH, 99.9%), L-arginine (99%), and deionized water (18 MΩ cm) were used. Two types of SiO<sub>2</sub> nanoparticles with distinct densities and porosities were synthesized using different growth mechanisms.

- (1) Particles of Type I (Shell-like) were obtained by regrowing of SiO<sub>2</sub> seeds in an alcohol–water–ammonia mixture using the modified Stober–Fink–Bohn method [55,56]. As a results of multistage growth process, 300-nm-diameter spherical SiO<sub>2</sub> particles, featuring a smooth surface, a shell-like internal structure, and deviations in particle diameter of <3% [57], were formed; see Figs. 2(a),(b).
- (2) Particles of Type II (Berry-like) were obtained by regrowing of SiO<sub>2</sub> seeds using the heterogeneous hydrolysis of TEOS in aqueous solution in the presence of L-arginine as a catalyst [58]. In order to regrow ~ 50-nm-diameter silica seeds to 300-nm-diameter particles, a portion of seeds was diluted with water-arginine solution (concentration of L-arginine was ~ 2 mM) and particle growth was carried out under constant stirring of a solution and at the temperature of 55 – 65°C, using a Elmi TW-2.02 magnetic stirrer with a water thermostat. A schematic and a SEM image of a typical 300-nm-diameter particle are shown in Figs. 2(c),(d).

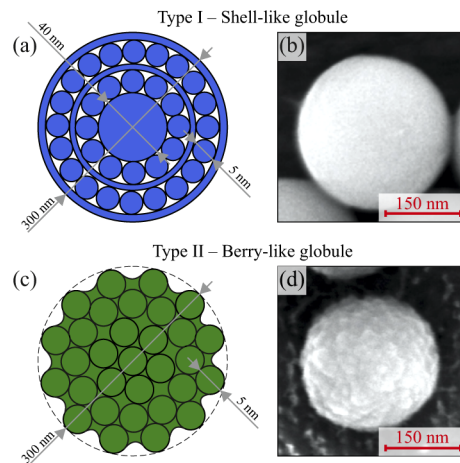


**Fig. 2.** Two types of 300-nm-diameter nanoporous SiO<sub>2</sub> globules used as basis for fabrication of the opal structures. (a),(b) A schematic and a SEM image of the Type I globule (Shell-like). (c),(d) Type II globule (Berry-like).

Notice, in order to objectively compare the two considered approaches of SiO<sub>2</sub> nanoparticles synthesis, in our experiments, we used the unitary particle diameter of 300 nm. First, this diameter is almost 3 orders smaller than the THz wavelengths, which allows us to prevent the Mie scattering effects, while THz-radiation transport in nanoporous SiO<sub>2</sub> can be described in the frameworks of the Rayleigh scattering theory and the effective medium theory. Second, such diameter appears to be quite technologically robust. Indeed, the particle of larger diameters would require much longer synthesis duration (especially, in case of using the heterogeneous hydrolysis of TEOS in aqueous solution [58]), while the particles of smaller diameter would require much longer time for the sedimentation of a colloidal suspension and the formation of a colloidal crystal.

Both approaches for synthesis of nanoporous SiO<sub>2</sub> globules appear to be rather technologically reliable. However, the Stober–Fink–Bohn method yields production of the “Shell-like” nanoparticles with a larger tunability of their diameter and porosity, as well as with higher growth rate, as compared to the heterogeneous hydrolysis of TEOS in aqueous solution. In this way, the Stober–Fink–Bohn method seems to be more promising for nanoporous SiO<sub>2</sub> application in THz optics, which demands for a large amount of particles in order to form large-scale bulk optical elements.

As illustrated in Fig. 3(a), opal structures were obtained by sedimentation of SiO<sub>2</sub> particles in an aqueous suspension. In Fig. 3(b), *in situ* photo of the sedimentation process is shown, while in Fig. 3(c), as-grown opal matrix with the diameter of 100 mm and the thickness of 10 mm is presented, where the Bragg scattering of visible light on the domains of ordered closely-packed particles is evident. In this way, a number of opal matrices were fabricated using two abovementioned types of SiO<sub>2</sub> particles.

Thus grown opal structures were then dried at the temperatures of 60 – 150 °C, in order to remove the residual water and to prevent cracking during the following high-temperature annealing [59]. Next, opals were annealed at different temperatures in the range of 200 – 1500 °C for 24 hours. Both drying and annealing were carried out using a resistive oven.

We then studied changes in the nanoporous SiO<sub>2</sub> structural properties as a function of annealing temperature using both the X-Ray diffractometer (DRON-4-07 with CuK $\alpha$  radiation and output monochromator) and the SEM imaging. For the two types of SiO<sub>2</sub> nanoparticles, the most pronounced changes in the material structure and density are observed for annealing temperatures

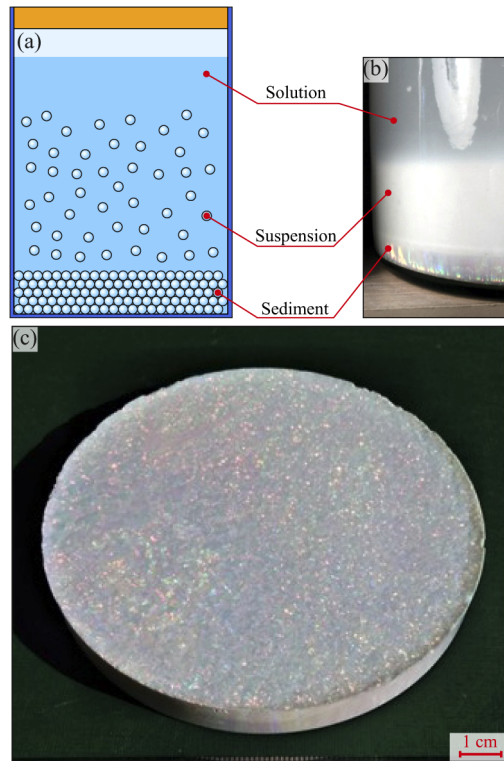


**Fig. 3.** Formation of the opal matrix by sedimentation and self-assembly of the  $\text{SiO}_2$  nanoparticles. (a),(b) A schematic and a photo of the sedimentation process. (c) A photo of the as-grown opal with the diameter of  $\sim 100$  mm and the thickness of  $\sim 10$  mm.

in the range of  $900 - 1200^\circ\text{C}$ . In Fig. 4, we present diffraction patterns and SEM images of the nanoporous  $\text{SiO}_2$  samples annealed at  $900$ ,  $1000$ ,  $1100$ , and  $1200^\circ\text{C}$ . From this data, we see that at higher annealing temperatures nanoporous  $\text{SiO}_2$  changes its phase state from amorphous  $\text{SiO}_2$  (see Figs. 4(a),(b) and (e),(f),(g)) to cristobalite (see Figs. 4(d),(e) and (h)). While the SEM images in panels (a),(e) show that the FCC lattice of colloidal crystal is still present, at the same time the SEM images from panels (b),(c) and (f),(g) show collapse of voids between the  $\text{SiO}_2$  globules. Finally, the SEM images in panels (d),(h) reveal a bulk structure of  $\text{SiO}_2$  for the annealing temperatures above  $1100 - 1200^\circ\text{C}$ . It is notable that phase and structural changes of the nanoporous  $\text{SiO}_2$  materials synthesized using different annealing temperatures depend on the type of globules used in their fabrication (Shell-like vs Berry-like). The observed differences between the "amorphous  $\text{SiO}_2 - \text{cristobalite}$ " phase transition temperatures for the two studied types of nanoporous  $\text{SiO}_2$  might originate from distinct porosity, surface energy and inner structure of nanoparticles. The latter factors can underlie differences between kinetic processes in these two media during their annealing. However, such dependence is difficult to quantify more systematically at this time, and more investigations are in order.

The dependence of the phase state and structure of the materials on annealing temperature also allows tuning of the material dielectric response at THz frequencies. In fact, the nanoporous materials feature a two-level porosity [53]. First, there are intraglobular pores (different for the two types of  $\text{SiO}_2$  globules used), and they collapse when annealing temperature reaches  $\sim 950^\circ\text{C}$ . Second, there are interglobular pores, that constitute  $\sim 30\%$  (by volume) of opal matrix and that collapse at the temperatures  $\sim 1000 - 1100^\circ\text{C}$ . While qualitative estimation of the total

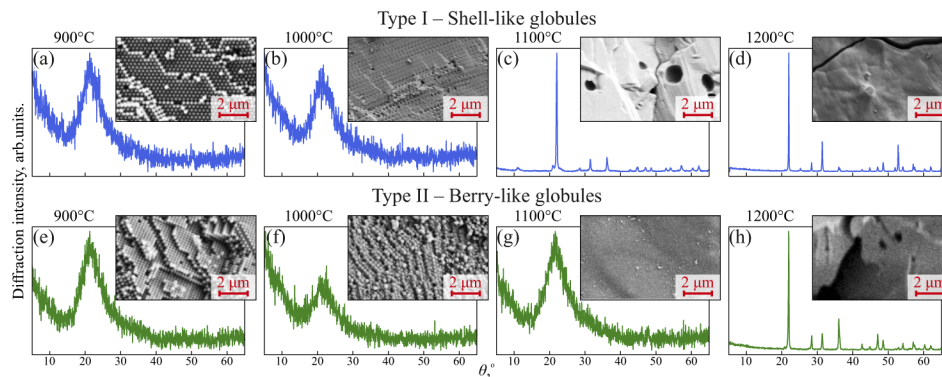


**Fig. 4.** Evolution of the structural properties of nanoporous  $\text{SiO}_2$  with increasing annealing temperature. (a)–(d) X-ray diffractometry of the nanoporous  $\text{SiO}_2$ , based on the Type I globules (Shell-like) annealed at the temperatures of 900, 1000, 1100, and 1200°C. Inserts represent SEM images of samples. (e)–(h) Nanoporous  $\text{SiO}_2$  samples, based on the Type II globules (Berry-like). Diffraction patterns in (a),(b) and (e),(f),(g) correspond to the amorphous  $\text{SiO}_2$ , while those in (c),(d) and (h) reveal cristobalite.

material porosity is detailed in what follows, here we note that ability of tuning the porosity across a wide range of values by annealing of nanoporous  $\text{SiO}_2$  is evident, thus, opening an opportunity of robust effective tuning of the THz optical properties of such materials.

Colloidal crystal obtained by sedimentation process usually possesses polycrystalline structure, in which dimensions of a crystalline domain can be roughly evaluated as a width of so-called "column" structures, clearly observed in Fig. 3(b) and (c). The domains in colloidal crystal are aligned in the direction of sedimentation (see Fig. 3(b)) and look like stars on the surface of as-grown opal (see Fig. 3(c)). Typical dimensions of such crystalline domains are in the range of  $\sim 0.1 - 1.0$  mm, being a function of the nanoparticle material and diameter, as well as of the technological parameters of sedimentation process. The effective optical properties of such an opal matrix can vary over its aperture due to the regions of less-packed particles at the interfaces between crystalline domains. At the same time, no pronounced fluctuations of the THz optical properties of opal were observed in our experiments, thus, the discussed material platform can be considered as a homogeneous one at the scale posed by THz wavelengths.

Moreover, thus considered material can be mechanically processed, which allows fabrication of THz bulk optics. That said, the mechanical processing strategy depends on the annealing temperature used and the material strength. For annealing temperatures in the range  $\sim 200 - 800^\circ\text{C}$ , the nanoporous  $\text{SiO}_2$  appears to be quite fragile. Therefore, for mechanical processing, the opal matrix should be first impregnated with some reinforcement substance, followed by its curing and the substance eventual removal after mechanical processing. For this purpose, paraffin, wax, or picein were used in this study. The reinforcing substance were then successfully removed from the opal matrix via moderate heating temperatures ( $<200^\circ\text{C}$ ) and evaporation, or by the sample ablation in an ultrasound bath with acetone, or by combining these two methods. The impregnation methods efficiently prevent damaging and cracking of the opals during standard mechanical processing without changing their nanostructure after removing the reinforcing substance. For annealing temperatures in the range  $\sim 900 - 1100^\circ\text{C}$ , the materials become strong enough for direct mechanical processing due to the formation of the solid bridges linking the individual globules in the opal matrix. For the temperatures  $>1100^\circ\text{C}$ , the materials become homogeneous and can be processed as a bulk glass.

To demonstrate mechanical robustness of the reported materials, samples of flat windows and lenses were fabricated from nanoporous  $\text{SiO}_2$  using grinding (see Fig. 5). In panels (a),(b),

significant change of nanoporous SiO<sub>2</sub> transmission and reflection properties in the visible range is notable, which also differs significantly for the two types of SiO<sub>2</sub> globules used in material synthesis. Thus the flat windows based on Type I globules (Shell-like) remain optically opaque regardless of the annealing temperature; this is due to the visible light scattering on pores, cracks and crystalline domains. In turn, the windows based of Type II globules (Berry-like) appear optically translucent in the visible range for the annealing temperature of 1100°C owing to suppressed Mie scattering on the structural inhomogeneities. A detailed analysis of this surprising effect is out of the scope of the current paper, and we defer its more detailed study to our future work.

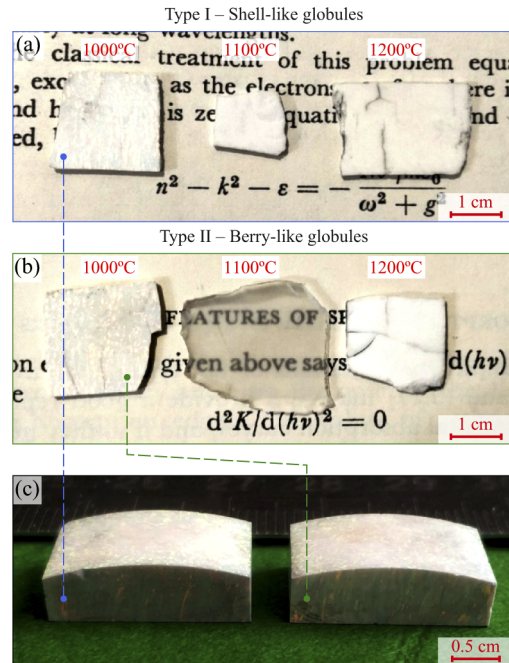


**Fig. 5.** Examples of the THz bulk optical elements fabricated from nanoporous SiO<sub>2</sub> using grinding. (a),(b) Flat 1-mm-thick windows made of nanoporous SiO<sub>2</sub> annealed at different temperatures, using Types I and II globules, respectively. (c) Plano-convex cylindrical lenses with the height of 6 mm, the width of 10 mm, and the radius of 30 mm, made of nanoporous SiO<sub>2</sub> using Type I and II globules, both annealed at 1000°C.

### 3. Terahertz pulsed spectroscopy of nanoporous SiO<sub>2</sub>

THz spectroscopy was performed using 1-mm-thick plates fabricated from both types of nanoporous SiO<sub>2</sub>, which were annealed at the temperatures in the range of 200 – 1500 °C. For each value of annealing temperature, 3 samples of nanoporous SiO<sub>2</sub> were used. The area of each sample was ~ 1 – 2 cm<sup>2</sup>. Typical sample plates are shown in Figs. 5(a),(b). The samples were characterized using an original THz pulsed spectrometer, described in Refs [60,61]. To reduce an impact of water vapor on the measured data, the THz beam path was placed under vacuum. Spectral operation range of our systems is 0.25 – 2.5 THz, while its spectral resolution is ~0.03 THz, as determined by the time-domain apodization of THz waveforms using the Tukey window with the width of 30 ps and the smoothness parameter of 0.1 [3]. The optical properties of nanoporous SiO<sub>2</sub> samples were reconstructed using an approach from Ref. [62], which relies on the plane wave approximation, takes into account finite number of satellite pulses in the THz

waveform, and yields a frequency-dependent complex refractive index

$$\tilde{n} = n - in'' \equiv n - i \frac{c_0}{2\pi\nu} \alpha, \quad (1)$$

where  $n$  and  $n''$  are its real and imaginary parts,  $c_0 = 3 \times 10^8$  m/s is the speed of light in a free space, and  $\alpha$  is a THz-wave absorption coefficient (by field).

In Fig. 6, the measured refractive index  $n$  and absorption coefficient  $\alpha$  are shown for the two types of SiO<sub>2</sub> globules and for different annealing temperatures. The markers correspond to mean values, while the error bars represent  $\pm 3\sigma$  confidential intervals of the measurements, where  $\sigma$  is a standard deviation, accounting for the optical properties variations within the considered set of samples. With increasing annealing temperature strong changes in the optical properties are observed –  $n$  increases from 1.65 to 1.95, and  $\alpha$  reduces from 10 to 1 cm<sup>-1</sup> at 1.0 THz, with a small differences for the Type I and Type II globules. For all samples, larger values of  $\alpha$  at higher frequencies are evident. Small group velocity dispersion at low frequencies is observed for samples annealed at low temperatures (<800 °C), which can be attributed to the bound water in the interglobular pores [6,46]. In turn, some group velocity dispersion at high frequencies, which is inherent for samples annealed at high temperatures (>1000 °C), might be attributed to the infrared excitations of SiO<sub>2</sub> crystalline phases [63,64]. The experimental data thus reveals an opportunity to tune the THz optical properties of nanoporous SiO<sub>2</sub> by annealing, while having low-to-moderate losses across the whole 0.25 – 2.5 THz range.

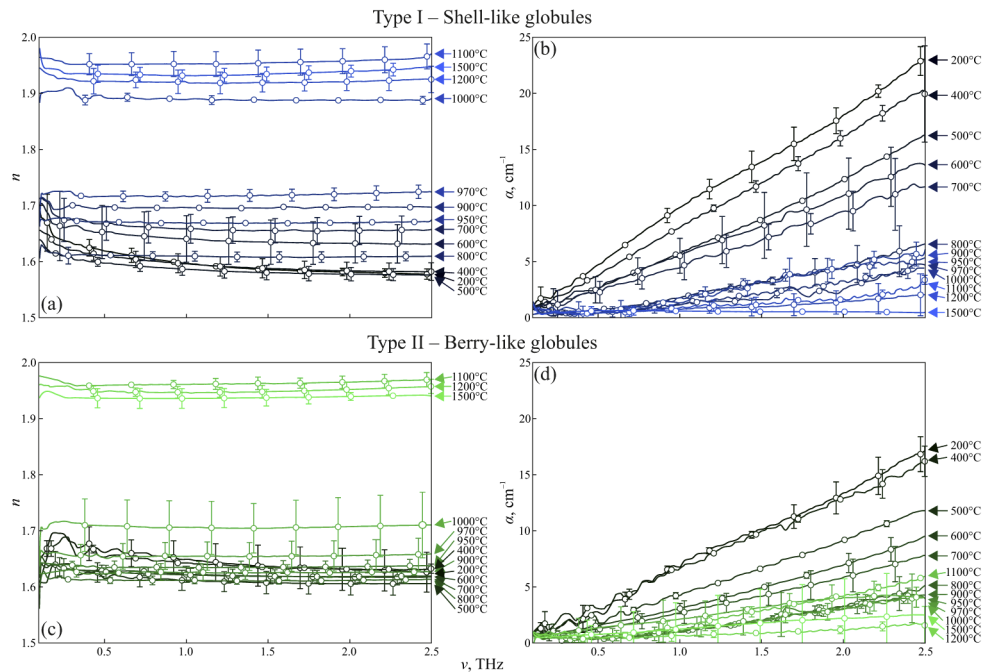


**Fig. 6.** THz refractive index  $n$  and absorption coefficient  $\alpha$  (by field) of nanoporous SiO<sub>2</sub> based on (a),(b) Type I globules (Shell-like) and (c),(d) Type II globules (Berry-like), annealed at different temperatures in the range of 200 – 1500 °C. Markers define mean values, while error bars represent  $\pm 3\sigma$  confidential intervals of measurements;  $\sigma$  is a standard deviation.

Tuning of the optical properties is possible due to changes in the material porosity, which we indicate as  $P$  in what follows. To quantify this statement, porosity was measured employing the hydrostatic weighting technique [65]. Particularly, water was used to infill the nanoporous



structures. Thanks to a low kinetic diameter of the H<sub>2</sub>O molecule (i.e.  $\sim 0.264$  nm) [66], it penetrates interglobular cavities with the dimensions as small as  $\sim 1$  nm. By neglecting the contribution of closed pores compared to the total porosity of the opal matrix (indeed, the amount of such pores is usually only 1 – 2%), the material porosity  $P$  is estimated as [65]

$$P = \frac{m_1 - m_0}{m_1 - m_2} \times 100\%, \quad (2)$$

where  $m_0$ ,  $m_1$ , and  $m_2$  are the masses of a dry porous sample in air, a sample infiltrated with liquid and suspended in air, and a sample infiltrated with liquid and suspended in liquid, respectively.

In Fig. 7, the optical properties  $n$ ,  $\alpha$  at 1.0 THz and the porosity  $P$  of nanoporous SiO<sub>2</sub> are shown, as a function of the annealing temperature  $T$ , for the Shell-like (a),(b) and Berry-like (c),(d) globules. With annealing temperature  $T$  increasing, porosity  $P$  reduces from  $\sim 40\%$  to 0, and only a small difference is observed for the two types of SiO<sub>2</sub> nanoparticles. For the opal structure based on the Shell-like globules, the maximal porosity  $P$  reaches  $\sim 41\%$ , composed of  $\sim 30\%$  interglobular porosity and  $\sim 11\%$  intraglobular porosity. In turn, for the opal structure based on the Berry-like globules, the porosity  $P$  can be as high as  $\sim 36\%$ , composed of  $\sim 30\%$  interglobular porosity and  $\sim 6\%$  intraglobular porosity. From Fig. 7(a),(c), an inverse relationship between  $n$  and  $P$  is evident. A reduction of porosity  $P$  with increasing annealing temperature in the 200 – 800 °C range is due to collapse of the interglobular pores, which results in the increasing refractive index  $n$ . In turn, annealing temperatures in the range of 800 – 1100 °C lead to abrupt reduction of porosity  $P$  due to collapse of the intraglobular pores (see Fig. 4), which results in the most pronounced increase of refractive index  $n$ . From Fig. 7(b),(d), a rapid drop of the material absorption coefficient  $\alpha$  is notable in the range below 800 – 900 °C, which can be attributed to collapse of the interglobular pores and to related evaporation of the residual bound water. Finally, a small increase of absorption  $\alpha$  at the annealing temperatures  $>1000$  °C can originate from the electro-dipole excitations of crystalline SiO<sub>2</sub> in the infrared range [63,64].

In order to qualitatively describe a relation between the THz optical properties and the porosity of nanoporous SiO<sub>2</sub>, we applied the Bruggeman effective medium theory [6]. In this way, nanoporous SiO<sub>2</sub> was treated as a mixture of its most dense state, observed at the highest annealing temperature (1500 °C), and of empty pores (free space). Knowing the temperature-dependent porosity  $P(T)$ , the complex dielectric permittivity of cristobalite  $\tilde{\epsilon}_{\text{SiO}_2} = \tilde{n}_{\text{SiO}_2}^2$  and free space  $\tilde{\epsilon}_{\text{air}} \equiv 1$ , the dielectric response of nanoporous SiO<sub>2</sub> can be calculated as a function of the annealing temperature  $\tilde{\epsilon}(T)$  by resolving the following equality

$$\frac{\tilde{\epsilon}_{\text{SiO}_2} - \tilde{\epsilon}(T)}{\tilde{\epsilon}_{\text{SiO}_2} + 2\tilde{\epsilon}(T)} (1 - P(T)) + \frac{1 - \tilde{\epsilon}(T)}{1 + 2\tilde{\epsilon}(T)} P(T) = 0, \quad (3)$$

while its complex refractive index is  $\tilde{n}(T) = \sqrt{\tilde{\epsilon}(T)}$ . In Fig. 7, we show (by solid lines) optical properties of the nanoporous SiO<sub>2</sub> estimated via Eq. (3) at 1.0 THz. An overall good agreement between the theoretical predictions and the experimental data is observed for both types of SiO<sub>2</sub> globules, especially at high annealing temperatures ( $>800$  °C). At low annealing temperatures, the observed differences between the Bruggeman model and the experiment are mostly due to unaccounted presence of the bound H<sub>2</sub>O molecules in pores of SiO<sub>2</sub> globules, which leads to increased experimental values of  $n$  and  $\alpha$ . High absorption of THz waves by nanoporous SiO<sub>2</sub> annealed at low temperatures ( $<800$  °C) limits the depth of their penetration in such a material by few millimeters and, thus, allows for fabrication of thin THz optical elements. In turn, nanoporous SiO<sub>2</sub> annealed at higher temperatures ( $>800$  °C) is favorable for fabrication of bulk THz optics.

It is worth noting that a contribution of these H<sub>2</sub>O molecules to formation of the nanoporous SiO<sub>2</sub> optical properties at THz frequencies is hard to be accounted in frameworks of the considered analytical Bruggeman effective medium model, since the dielectric response of such bound and segregated water depends on a number of factors and usually strongly differs from that of a bulk

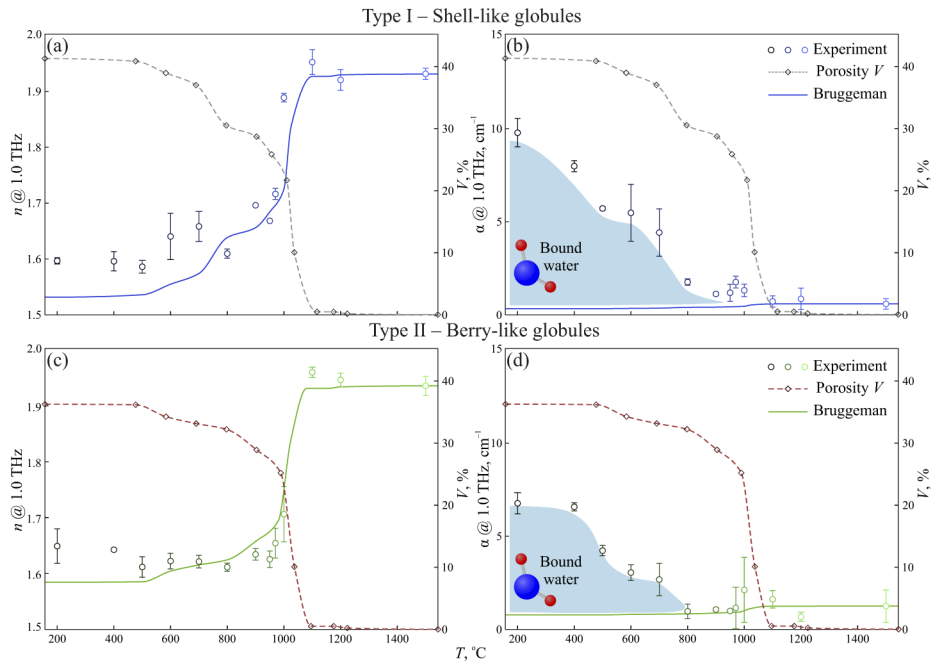


**Fig. 7.** The measured porosity  $V$  (dashed line), refractive index  $n$  (markers) and absorption coefficient  $\alpha$  (markers) at 1.0 THz, as well as the Bruggeman model (Eq. (7)) of effective dielectric response (solid lines) for nanoporous  $\text{SiO}_2$  based on (a),(b) the Type I globules (Shell-like) and (c),(d) the Type II globules (Berry-like), annealed at different temperatures  $T$ . Error bars in the experimental data for  $n$  and  $\alpha$  represent  $\pm 3\sigma$  confidential interval of measurements.

one [6,67–69]. The developed model also does not account for structural phase transitions in the nanoporous  $\text{SiO}_2$ , which can also be a reason for the observed differences and which limits applicability of the developed model to the considered spectral range only. Nevertheless, it gives us a favorable practical relation, which can be applied for predicting the THz optical properties of nanoporous  $\text{SiO}_2$  and which would be used in synthesis and fabrication of THz optics.

Finally, from Figs. 7(b),(d) one notes that the Type II globules (Berry-like) results in lower THz-wave absorption at small annealing temperatures ( $<800^\circ\text{C}$ ) and, thus contains a lower amount of bound water than that in Type I nanoparticles (Shell-like), which is expected. Thus, nanoporous  $\text{SiO}_2$  based on the Berry-like globules appears to be more attractive when synthesized using lower annealing temperatures.

#### 4. Discussions

The developed material platform is highly relevant for the fabrication of bulk THz optical components thanks to the tunability of the nanoporous  $\text{SiO}_2$  effective THz optical properties, its low loss, as well as high tolerance to the mechanical processing. In addition to the direct mechanical processing of opals, it is also possible to fabricate opal-based optical elements by direct sedimentation of the colloidal particles into a cast of the required shape. This technique opens new ways for the fabrication of both the bulk optical elements and the antireflection coatings. However, we postpone a study of this technique to our future work.

The developed material platform can be further enhanced. Thus, optical properties of the nanoporous  $\text{SiO}_2$  can be varied in a wide range by its impregnation with liquid polymers/monomers (followed by curing), or with high-refractive index dielectric, magnetic, or metal (plasmonic)

nanoparticles [42,70–72]. Magnetic particles can lead to appearance of magnetic resonances in the optical properties of the modified materials in the THz and GHz ranges, while plasmonic resonances in the visible ranges can further increase effective refractive index of the composite materials even at low frequencies (including the THz range), as follows from the Kramers-Kronig relations [73]. Furthermore, using colloidal SiO<sub>2</sub> nanoparticles with different diameters or their agglomerates (i.e. microspheres [52]), or using nanoparticles made of other common materials (such as PolyMethylMethAcrylate (PMMA) or Melamine Formaldehyde (MF)) can result in novel opal structures with unusual optical and mechanical properties. However, such materials might require completely different thermo-mechanical regimes. Other option is to use inverse opals [74–76], fabricated by filling the interglobular pores of opal matrix by some substance followed by etching of SiO<sub>2</sub> globules with hydrofluoric acid, as a perspective THz optical material with a very high porosity (>70%) and, thus, a very small effective refractive index. The developed material platform can also open opportunities in advanced multispectral applications, where judiciously designed dielectric properties are required at both THz frequencies and in the visible and infrared ranges [54].

Finally, the effects of structural changes and phase transitions in nanoporous SiO<sub>2</sub> on its optical properties deserve further studies (see Figs. 4, 6, and 7), which we refer to our future work.

## 5. Conclusions

In this work, THz optical properties of the artificial opals, made of two different types of nanoporous SiO<sub>2</sub> globules were studied as a function of the annealing temperature. We found that when increasing annealing temperature, refractive index of nanoporous SiO<sub>2</sub> increases from 1.6 to 1.95, while its absorption coefficient (by amplitude) reduces from 10 to 1 cm<sup>-1</sup> at 1.0 THz. A theoretical model describing evolution of the nanoporous SiO<sub>2</sub> optical properties, as a function of the material porosity and the annealing temperature, was proposed using the Bruggeman effective medium theory. The highly designable optical properties, along with relatively low THz-wave material absorption, as well as mechanical robustness, make the nanoporous SiO<sub>2</sub> a promising material platform for THz optics.

## Funding

Russian Science Foundation (19-12-00402); Canada Research Chairs (Ubiquitous Terahertz Photonics Project).

## Acknowledgements

The work on synthesis of colloidal nanoparticles, fabrication, structural characterization and THz pulsed spectroscopy of nanoporous SiO<sub>2</sub> samples by V.E. Ulitko, G.M. Katyba, V.N. Kurlov, V.M. Masalov and I.N. Dolganova was supported by the grant from the Russian Science Foundation (RSF), Project # 19-12-00402. Analysis of the THz optical properties of nanoporous SiO<sub>2</sub> samples by M. Skorobogatiy was supported by the Ubiquitous Terahertz Photonics Project, the Canada Research Chairs Program.

## Disclosures

The authors declare no conflicts of interest.

## References

1. H. Guerboukha, K. Nallappan, and M. Skorobogatiy, "Toward real-time terahertz imaging," *Adv. Opt. Photonics* **10**(4), 843–938 (2018).
2. C. Walker, *Terahertz Astronomy*. 1st Edition (CRC Press, 2015).

3. B. Giuliano, A. Gavdush, B. Müller, K. Zaytsev, T. Grassi, A. Ivlev, M. Palumbo, G. Baratta, C. Scirè, G. Komandin, S. Yurchenko, and P. Caselli, "Broadband spectroscopy of astrophysical ice analogues - I. Direct measurement of the complex refractive index of CO ice using terahertz time-domain spectroscopy," *Astron. Astrophys.* **629**, A112 (2019).
4. D. Shao, P. Yotprayoonsak, V. Saunajoki, M. Ahlskog, J. Virtanen, V. Kangas, A. Volodin, C. V. Haesendonck, M. Burdanova, C. D. W. Mosley, and J. Lloyd-Hughes, "Conduction properties of thin films from a water soluble carbon nanotube/hemicellulose complex," *Nanotechnology* **29**(14), 145203 (2018).
5. M. Burdanova, A. Tsapenko, D. Satco, R. Kashtiban, C. Mosley, M. Monti, M. Staniforth, J. Sloan, Y. Gladush, A. Nasibulin, and J. Lloyd-Hughes, "Giant negative terahertz photoconductivity in controllably doped carbon nanotube networks," *ACS Photonics* **6**(4), 1058–1066 (2019).
6. O. Smolyanskaya, N. Chernomyrdin, A. Konovko, K. Zaytsev, I. Ozheredov, O. Cherkasova, M. Nazarov, J.-P. Guillet, S. Kozlov, Y. Kistenev, J.-L. Coutaz, P. Mounaix, V. Vaks, J.-H. Son, H. Cheon, V. Wallace, Y. Feldman, I. Popov, A. Yaroslavsky, A. Shkurinov, and V. Tuchin, "Terahertz biophotonics as a tool for studies of dielectric and spectral properties of biological tissues and liquids," *Prog. Quantum Electron.* **62**, 1–77 (2018).
7. K. Zaytsev, I. Dolganova, N. Chernomyrdin, G. Katyba, A. Gavdush, O. Cherkasova, G. Komandin, M. Shchedrina, A. Khodan, D. Ponomarev, I. Reshetov, V. Karasik, M. Skorobogatiy, V. Kurlov, and V. Tuchin, "The progress and perspectives of terahertz technology for diagnosis of neoplasms: a review," *J. Opt.* **22**(1), 013001 (2019).
8. I. Dolganova, K. Zaytsev, S. Yurchenko, V. Karasik, and V. Tuchin, "The role of scattering in quasi-ordered structures for terahertz imaging: Local order can increase an image quality," *IEEE Trans. Terahertz Sci. Technol.* **8**(4), 403–409 (2018).
9. Y. Tao, A. Fitzgerald, and V. Wallace, "Non-contact, non-destructive testing in various industrial sectors with terahertz technology," *Sensors* **20**(3), 712 (2020).
10. J. Zeitler, P. Taday, D. Newnham, M. Pepper, K. Gordon, and T. Rades, "Terahertz pulsed spectroscopy and imaging in the pharmaceutical setting - a review," *J. Pharm. Pharmacol.* **59**(2), 209–223 (2007).
11. A. Ren, A. Zahid, D. Fan, X. Yang, M. I. Ali, A. Alomainy, and Q. Abbasi, "State-of-the-art in terahertz sensing for food and water security – a comprehensive review," *Trends Food Sci. Technol.* **85**, 241–251 (2019).
12. S. Lepeshov, A. Gorodetsky, A. Krasnok, E. Rafailov, and P. Belov, "Enhancement of terahertz photoconductive antenna operation by optical nanoantennas," *Laser Photonics Rev.* **11**(1), 1770001 (2017).
13. A. Yachmenev, D. Lavrukhin, I. Glinskiy, N. Zenchenko, Y. Goncharov, I. Spektor, R. Khabibullin, T. Otsuji, and D. Ponomarev, "Metallic and dielectric metasurfaces in photoconductive terahertz devices: a review," *Opt. Eng.* **59**(6), 061608 (2019).
14. M. Morozov, V. Leiman, V. Popov, V. Mitin, M. Shur, V. Karasik, M. Ryzhii, T. Otsuji, and V. Ryzhii, "Optical pumping in graphene-based terahertz/far-infrared superluminescent and laser heterostructures with graded-gap black-P<sub>x</sub>As<sub>1-x</sub> absorbing-cooling layers," *Opt. Eng.* **59**(6), 061606 (2019).
15. A. Yachmenev, S. Pushkarev, R. Reznik, R. Khabibullin, and D. Ponomarev, "Arsenides and related III–V materials-based multilayered structures for terahertz applications," *Prog. Cryst. Growth Charact. Mater.* **6**(2), 100485 (2020).
16. Q. Sun, X. Chen, X. Liu, R. Stantchev, and E. Pickwell-MacPherson, "Exploiting total internal reflection geometry for terahertz devices and enhanced sample characterization," *Adv. Opt. Mater.* **8**(3), 1900535 (2020).
17. M. Manjappa and R. Singh, "Materials for terahertz optical science and technology," *Adv. Opt. Mater.* **8**(3), 1901984 (2020).
18. M. Islam, C. Cordeiro, M. Franco, J. Sultana, A. Cruz, and D. Abbott, "Terahertz optical fibers," *Opt. Express* **28**(11), 16089–16117 (2020).
19. S. Grischkowsky, S. Keiding, M. van Exter, and C. Fattinger, "Far-infrared time-domain spectroscopy with terahertz beams of dielectrics and semiconductors," *J. Opt. Soc. Am. B* **7**(10), 2006–2015 (1990).
20. A. Podzorov and G. Gallot, "Low-loss polymers for terahertz applications," *Appl. Opt.* **47**(18), 3254–3257 (2008).
21. S. Atakaramians, S. Afshar, T. Monroe, and D. Abbott, "Terahertz dielectric waveguides," *Adv. Opt. Photonics* **5**(2), 169–215 (2013).
22. B. Scherger, M. Scheller, C. Jansen, M. Koch, and K. Wiesauer, "Terahertz lenses made by compression molding of micropowders," *Appl. Opt.* **50**(15), 2256–2262 (2011).
23. K. Nielsen, H. Rasmussen, P. Uhd Jepsen, and O. Bang, "Porous-core honeycomb bandgap THz fiber," *Opt. Lett.* **36**(5), 666–668 (2011).
24. H. Bao, K. Nielsen, H. Rasmussen, P. Uhd Jepsen, and O. Bang, "Fabrication and characterization of porous-core honeycomb bandgap THz fibers," *Opt. Express* **20**(28), 29507–29517 (2012).
25. T. Ma, A. Markov, L. Wang, and M. Skorobogatiy, "Graded index porous optical fibers – dispersion management in terahertz range," *Opt. Express* **23**(6), 7856–7869 (2015).
26. F. Zhou, W. Cao, B. Dong, T. Reissman, W. Zhang, and C. Sun, "Additive manufacturing of a 3D terahertz gradient-refractive index lens," *Adv. Opt. Mater.* **4**(7), 1034–1040 (2016).
27. J. Li, K. Nallappan, H. Guerboukha, and M. Skorobogatiy, "3D printed hollow core terahertz bragg waveguides with defect layers for surface sensing applications," *Opt. Express* **25**(4), 4126–4144 (2017).
28. M. Nazarov, A. Shilov, K. Bzheumikhov, Z. Margushev, V. Sokolov, A. Sotsky, and A. Shkurinov, "Eight-capillary cladding thz waveguide with low propagation losses and dispersion," *IEEE Trans. Terahertz Sci. Technol.* **8**(2), 183–191 (2018).
29. T. Ma, H. Guerboukha, M. Girard, A. Squires, R. Lewis, and M. Skorobogatiy, "3d printed hollow-core terahertz optical waveguides with hyperuniform disordered dielectric reflectors," *Adv. Opt. Mater.* **4**(12), 2085–2094 (2016).

30. H. Guerboukha, K. Nallappan, Y. Cao, M. Seghilani, J. Azaña, and M. Skorobogatiy, "Planar porous components for low-loss terahertz optics," *Adv. Opt. Mater.* **7**(15), 1900236 (2019).
31. A. Dupuis, A. Mazhorova, F. Desevedavy, M. Roze, and M. Skorobogatiy, "Spectral characterization of porous dielectric subwavelength THz fibers fabricated using a microstructured molding technique," *Opt. Express* **18**(13), 13813–13828 (2010).
32. B. Chalmers, H. LaBelle, and A. Mlavsky, "Edge-defined, film-fed crystal growth," *J. Cryst. Growth* **13-14**, 84–87 (1972).
33. P. Antonov and V. Kurlov, "A review of developments in shaped crystal growth of sapphire by the Stepanov and related techniques," *Prog. Cryst. Growth Charact. Mater.* **44**(2), 63–122 (2002).
34. N. Abrosimov, V. Kurlov, and S. Rossolenko, "Automated control of Czochralski and shaped crystal growth processes using weighing techniques," *Prog. Cryst. Growth Charact. Mater.* **46**(1-2), 1–57 (2003).
35. G. Katyba, K. Zaytsev, I. Dolganova, I. Shikunova, N. Chernomyrdin, S. Yurchenko, G. Komandin, I. Reshetov, V. Nesvizhevsky, and V. Kurlov, "Sapphire shaped crystals for waveguiding, sensing and exposure applications," *Prog. Cryst. Growth Charact. Mater.* **64**(4), 133–151 (2018).
36. G. Katyba, K. Zaytsev, N. Chernomyrdin, I. Shikunova, G. Komandin, V. Anzin, S. Lebedev, I. Spektor, V. Karasik, S. Yurchenko, I. Reshetov, V. Kurlov, and M. Skorobogatiy, "Sapphire photonic crystal waveguides for terahertz sensing in aggressive environments," *Adv. Opt. Mater.* **6**(22), 1800573 (2018).
37. I. Minin, O. Minin, G. Katyba, N. Chernomyrdin, V. Kurlov, K. Zaytsev, L. Yue, Z. Wang, and D. Christodoulides, "Experimental observation of a photonic hook," *Appl. Phys. Lett.* **114**(3), 031105 (2019).
38. K. Zaytsev, G. Katyba, N. Chernomyrdin, I. Dolganova, A. Rossolenko, V. Tuchin, V. Kurlov, and M. Skorobogatiy, "Overcoming the Abbe diffraction limit using a bundle of metal-coated high-refractive-index sapphire optical fibers," *Adv. Opt. Mater.* **2020**, 2000307 (2020).
39. D. Han, K. Lee, J. Lim, S. Hong, Y. Kim, and J. Ahn, "Terahertz lens made out of natural stone," *Appl. Opt.* **52**(36), 8670–8675 (2013).
40. M. Nazarov, E. Khaydukov, A. Savelyev, V. Sokolov, A. Akhmanov, A. Shkurinov, and V. Panchenko, "Terahertz response of a polymer composite with high concentration of silicon micro- and nanoparticles," *Nanotechnol. Russ.* **10**(3-4), 247–253 (2015).
41. M. Wichmann, A. Mondol, N. Kocic, S. Lippert, T. Probst, M. Schwerdtfeger, S. Schumann, T. Hochrein, P. Heidemeyer, M. Bastian, G. Bastian, and M. Koch, "Terahertz plastic compound lenses," *Appl. Opt.* **52**(18), 4186–4191 (2013).
42. M. Sindler, C. Kadlec, F. Dominec, P. Kuzel, C. Elissalde, A. Kassas, J. Lesseur, D. Bernard, P. Mounaix, and H. Nemeč, "Bulk magnetic terahertz metamaterials based on dielectric microspheres," *Opt. Express* **24**(16), 18340–18345 (2016).
43. A. Nakanishi and H. Satozono, "Terahertz optical properties of wood–plastic composites," *Appl. Opt.* **59**(4), 904–909 (2020).
44. H. Guerboukha, G. Yan, O. Skorobogata, and M. Skorobogatiy, "Silk foam terahertz waveguides," *Adv. Opt. Mater.* **2**(12), 1181–1192 (2014).
45. J. Zhang and D. Grischkowsky, "Terahertz time-domain spectroscopy study of silica aerogels and adsorbed molecular vapors," *J. Phys. Chem. B* **108**(48), 18590–18600 (2004).
46. G. Komandin, V. Nozdrin, A. Gavdush, A. Pronin, O. Porodinkov, I. Spektor, V. Sigaev, A. Mikhailov, G. Shakhgildyan, V. Ulitko, and D. Abdullaev, "Effect of moisture adsorption on the broadband dielectric response of SiO<sub>2</sub>-based nanoporous glass," *J. Appl. Phys.* **126**(22), 224303 (2019).
47. C. Simovski, P. Belov, A. Atrashchenko, and Y. Kivshar, "Wire metamaterials: Physics and applications," *Adv. Mater.* **24**(31), 4229–4248 (2012).
48. A. Tuniz, B. Kuhlmeier, R. Lwin, A. Wang, J. Anthony, R. Leonhardt, and S. Fleming, "Drawn metamaterials with plasmonic response at terahertz frequencies," *Appl. Phys. Lett.* **96**(19), 191101 (2010).
49. M. Habib, A. Stefani, S. Atakaramians, S. Fleming, A. Argyros, and B. Kuhlmeier, "A prism based magnifying hyperlens with broad-band imaging," *Appl. Phys. Lett.* **110**(10), 101106 (2017).
50. M. Komlenok, S. Tikhodeev, T. Weiss, S. Lebedev, G. Komandin, and V. Konov, "All-carbon diamond/graphite metasurface: Experiment and modeling," *Appl. Phys. Lett.* **113**(4), 041101 (2018).
51. M. Komlenok, S. Lebedev, G. Komandin, A. Pique, and V. Konov, "Fabrication and electrodynamic properties of all-carbon terahertz planar metamaterials by laser direct-write," *Laser Phys. Lett.* **15**(3), 036201 (2018).
52. A. Zhokhov, V. Masalov, N. Sukhinina, D. Matveev, P. Dolganov, V. Dolganov, and G. Emelchenko, "Photonic crystal microspheres," *Opt. Mater.* **49**, 208–212 (2015).
53. V. Somenkov, S. Agafonov, M. Shushunov, V. Filonenko, V. Masalov, and G. Emelchenko, "Phase transformations in opals under thermal and thermobaric actions," *J. Surf. Invest.: X-Ray, Synchrotron Neutron Tech.* **11**(3), 634–638 (2017).
54. S. Yurchenko, K. Zaytsev, E. Gorbunov, E. Yakovlev, A. Zotov, V. Masalov, G. Emelchenko, and V. Gorelik, "Enhanced third-harmonic generation in photonic crystals at band-gap pumping," *J. Phys. D: Appl. Phys.* **50**(5), 055105 (2017).
55. K. Hartlen, A. T. Athanasopoulos, and V. Kitaev, "Facile Preparation of Highly Monodisperse Small Silica Spheres (15 to >200 nm) Suitable for Colloidal Templating and Formation of Ordered Arrays," *Langmuir* **24**(5), 1714–1720 (2008).

56. V. Masalov, N. Sukhinina, and G. Emelchenko, "Colloidal particles of silicon dioxide or the formation of opal-like structures," *Phys. Solid State* **53**(6), 1135–1139 (2011).
57. V. Masalov, E. Kudrenko, N. Grigoryeva, K. Ezdakova, V. Roddatis, N. Sukhinina, M. Arefev, A. Mistonov, S. Grigoriev, and G. Emelchenko, "Direct observation of the shell-like structure of SiO<sub>2</sub> particles synthesized by the multistage Stober method," *Nano* **08**(04), 1350036 (2013).
58. V. Masalov, N. Sukhinina, and G. Emelchenko, "Synthesis of monodisperse silica nanoparticles via heterogeneous tetraethoxysilane hydrolysis using l-arginine as a catalyst," *Inorg. Mater.* **54**(2), 156–162 (2018).
59. V. Masalov, A. Zotov, P. Dolganov, N. Sukhinina, and G. Emelchenko, "Effect of heat treatment on water vapor adsorption by opal structures and their effective refractive index," *Inorg. Mater.* **55**(2), 143–148 (2019).
60. D. Lavrukhin, A. Yachmenev, A. Pavlov, R. Khabibullin, Y. Goncharov, I. Spektor, G. Komandin, S. Yurchenko, N. Chernomyrdin, K. Zaytsev, and D. Ponomarev, "Shaping the spectrum of terahertz photoconductive antenna by frequency-dependent impedance modulation," *Semicond. Sci. Technol.* **34**(3), 034005 (2019).
61. G. Komandin, V. Anzin, V. Ulitko, A. Gavdush, A. Mukhin, Y. Goncharov, O. Porodinkov, and I. Spektor, "Optical cryostat with sample rotating unit for polarization-sensitive terahertz and infrared spectroscopy," *Opt. Eng.* **59**(6), 061603 (2020).
62. K. Zaytsev, A. Gavdush, V. Karasik, V. Alekhnovich, P. Nosov, V. Lazarev, I. Reshetov, and S. Yurchenko, "Accuracy of sample material parameters reconstruction using terahertz pulsed spectroscopy," *J. Appl. Phys.* **115**(19), 193105 (2014).
63. M. Nabil, K. R. Mahmoud, A. El-Shaer, and H. A. Nayber, "Preparation of crystalline silica (quartz, cristobalite, and tridymite) and amorphous silica powder (one step)," *J. Phys. Chem. Solids* **121**, 22–26 (2018).
64. A. Akane, O. Masayuki, O. Hiroki, M. Tomoyuki, A. Shoji, K. Shin'ichi, K. Mikio, and I. Nobuaki, "Structural changes of synthetic opal by heat treatment," *Phys. Chem. Miner.* **40**(9), 747–755 (2013).
65. E. Samarov, A. Mokrushin, V. Masalov, G. Abrosimova, and G. Emelchenko, "Structural modification of synthetic opals during thermal treatment," *Phys. Solid State* **48**(7), 1280–1283 (2006).
66. F. Ismail, K. Khulbe, and T. Matsuura, *Gas Separation Membranes* (Springer, 2015).
67. S. Yurchenko and K. Zaytsev, "Spectroscopy of nafion in terahertz frequency range," *J. Appl. Phys.* **116**(11), 113508 (2014).
68. M. Belyanchikov, E. Zhukova, S. Tretiak, A. Zhugayevych, M. Dressel, F. Uhlig, J. Smiatek, M. Fyta, V. Thomas, and B. Gorshunov, "Vibrational states of nano-confined water molecules in beryl investigated by first-principles calculations and optical experiments," *Phys. Chem. Chem. Phys.* **19**(45), 30740–30748 (2017).
69. O. Cherkasova, M. Nazarov, M. Konnikova, and A. Shkurinov, "Thz spectroscopy of bound water in glucose: Direct measurements from crystalline to dissolved state," *Journal of Infrared Millimeter and Terahz Waves* <https://doi.org/10.1007/s10762-020-00684-4> (2020).
70. A. Nistler, C. Hartmann, C. Rumenapp, M. Opel, B. Gleich, N. P. Ivleva, R. Niessner, and M. Seidel, "Production and characterization of long-term stable superparamagnetic iron oxide-shell silica-core nanocomposites," *J. Magn. Mater.* **442**, 497–503 (2017).
71. V. Khanadeev, B. Khlebtsov, S. Klimova, M. Tsvetkov, V. Bagratashvili, G. Sukhorukov, and N. Khlebtsov, "Large-scale high-quality 2D silica crystals: dip-drawing formation and decoration with gold nanorods and nanospheres for SERS analysis," *Nanotechnology* **25**(40), 405602 (2014).
72. L. Dykman and N. Khlebtsov, "Methods for chemical synthesis of colloidal gold," *Russ. Chem. Rev.* **88**(3), 229–247 (2019).
73. P. Martin, "Sum rules, Kramers-Kronig relations, and transport coefficients in charged systems," *Phys. Rev.* **161**(1), 143–155 (1967).
74. V. Masalov, P. Dolganov, N. Sukhinina, V. Dolganov, and G. Emelchenko, "Synthesis of polymer - based inverted opal and transformation of its optical properties," *Adv. Nano. Res.* **2**(1), 69–76 (2014).
75. P. Dolganov, V. Masalov, N. Sukhinina, V. Dolganov, and G. Emel'chenko, "Inverse opal based on a polymer filler and transformation of its optical characteristics," *Phys. Solid State* **56**(4), 746–750 (2014).
76. N. Sukhinina, V. Masalov, A. Zhokhov, I. Zverkova, Q. Liu, J. Wang, and G. Emelchenko, "Synthesis, structure, and electrochemical characteristics of carbon inverse opals," *Inorg. Mater. Appl. Res.* **9**(1), 92–99 (2018).